(This is a sample cover image for this issue. The actual cover is not yet available at this time.)

Earth and Planetary Science Letters 361 (2013) 120–133

Contents lists available at SciVerse ScienceDirect

Earth and Planetary Science Letters

journal homepage: www.elsevier.com/locate/epsl

On the origin of hot metasedimentary quartzites in the lower crust of continental arcs

Emily J. Chin [a,*], Cin-Ty A. Lee [a], Darren L. Tollstrup [b], Liewen Xie [c], Josh B. Wimpenny [b], Qing-Zhu Yin [b]

[a] Department of Earth Science, Rice University, Houston, TX 77005, USA
[b] Department of Geology, University of California Davis, Davis, CA 95616, USA
[c] State Key Laboratory of Lithospheric Evolution, Institute of Geology and Geophysics, Chinese Academy of Sciences, Beijing 100029, China

ARTICLE INFO

Article history:
Received 24 March 2012
Received in revised form
12 November 2012
Accepted 15 November 2012
Editor: T.M. Harrison

Keywords:
continental arc
detrital zircon
granulite
Sierra Nevada
miogeocline
passive margin

ABSTRACT

Volcanic arcs associated with subduction zones are thought to be the primary building blocks of continents. The composition of the magmas, particularly in continental arcs, is the product of mixing between differentiation of juvenile magmas and pre-existing crustal wallrock, the former being typically mafic and the latter more silicic. Because the upper continental crust is on average thought to be more silicic than the mafic lower crust, mixing with silicic endmembers should occur primarily in the upper crust. However, we show here that the lower crust of continental arcs contains silicic metasediments. We examine garnet-bearing, granulite-facies sedimentary quartzite xenoliths from the Sierra Nevada batholith in California, a Cretaceous continental arc. The quartzites have equigranular textures and contain quartz ($>50\%$), plagioclase ($<30\%$), garnet (10%), and small amounts ($<1\%$) of rutile, aluminosilicate, biotite, monazite, zircon, graphite and trace orthopyroxene. Cathodoluminescent images show zircons with rounded detrital cores mantled by metamorphic overgrowths. Hf isotopic model ages and U–Pb upper intercept ages, for a given zircon, are similar, but the zircon population shows variable protolith ages ranging from Proterozoic to Archean. In contrast, all zircons share similar lower intercept U–Pb ages (103 ± 10 Ma), which coincide with the peak of arc magmatism in the Sierra Nevada. The Precambrian protolith ages are similar to North American cratonal basement, and together with the abundance of quartz and detrital zircons, suggest that these quartzites represent ancient, passive margin sediments instead of juvenile active margin sediments in the oceanic trench and accretionary prism. Importantly, these quartzites record peak metamorphic temperatures and pressures of 700–800 °C using Ti-in-quartz thermometry and 0.7–1.1 GPa using garnet–aluminosilicate–plagioclase thermobarometry, indicating that these xenoliths experienced significant heating and possible partial melting in the lower crust, most likely related to arc magmatism as suggested by similarities between the lower intercept U–Pb ages and the ages of plutonism in the Sierra Nevada. Possible mechanisms by which these sediments were transported into the lower crust include continental underthrusting beneath the continental arc, underplating by buoyant slab-derived sedimentary diapirs, or viscous downflow of country rock in response to diapiric ascent of plutons. Continental underthrusting has been independently documented during the Sevier orogeny, coinciding with the peak of arc magmatism. We thus speculate that supracrustal rocks may have been underthrusted into deep crustal magmatic zones. Regardless of how these metasediments arrived in the lower crust, our observations indicate that silicic metasediments occur in the lower crust of volcanic arcs, not just in the upper crust as is commonly thought. Transport of metasediments into deep crustal magmatic zones should influence the composition of arc magmas and continental crust in general.

1. Introduction

Arc magmas formed above subduction zones are considered to be essential components in building continents. The compositional stratification of continental crust, from felsic upper crust grading into mafic lower crust, is attained through a combination of igneous differentiation and interaction of juvenile arc magmas with pre-existing wallrocks (Hildreth, 1981; Hildreth and Moorbath, 1988). Fractional crystallization of a basaltic melt results in the retention of dense, mafic cumulates in the deep lithosphere, leaving the residual felsic melts to escape to shallower crustal levels owing to their lower densities. Further refinement of magmas in the upper crust may also involve mixing with pre-existing wallrocks, which are typically felsic.

In this study, we present evidence for silicic metasedimentary rocks in the lower crust of a mature continental arc, the Sierra Nevada Batholith in California. The metasediments are nearly

* Corresponding author.
E-mail address: ejc5@rice.edu (E.J. Chin).

0012-821X/$ - see front matter © 2012 Elsevier B.V. All rights reserved.
http://dx.doi.org/10.1016/j.epsl.2012.11.031

pure quartzite or metasandstone xenoliths (>85 wt% SiO_2). They contain metamorphic garnet and last equilibrated within the granulite facies, recording temperatures in excess of 700 °C and pressures of 1 GPa. Upper intercepts of U–Pb discordia and Hf isotope systematics in detrital zircons show that the metasediments represent strata of the ancient passive margin of North America. Detrital zircon cores are rimmed by metamorphic overgrowths, which yield a common U–Pb lower intercept age coeval with the Late Cretaceous peak of arc magmatism in the Sierra Nevada.

Such quartz-rich sediments are anomalous in the mafic lower crust, suggesting that they were transported from their origin in shallow passive margin depocenters into the deep crust. We propose continental underthrusting as one mechanism, but explore other hypotheses, such as wallrock downwelling associated with plutons rising into the crust and underplating by sediment diapirs derived from the subducting slab. The Sierran lower crustal quartzites offer a unique window into the lower crust, and regardless of the mechanism of their emplacement, indicate that the lower crust may be more felsic than previously thought.

2. Geologic setting

During the Paleozoic, the western margin of North America was defined by a passive margin. In the early Mesozoic, island arcs and other exotic terranes were accreted on to this margin (Dickinson, 1981). This transition in tectonic environment was manifested as two distinct Cordilleran depositional settings: mature passive margin sediments (historically referred to as "miogeoclinal") deposited in the Paleozoic, and juvenile ("eugeoclinal") sediments associated with the Mesozoic active margin (Kistler, 1990; Moore and Foster, 1980; Stewart, 1970). The passive margin sediments formed a westward thickening wedge of siliciclastics and carbonates extending from eastern Utah to southwestern Nevada and eastern California. Its maximum estimated thickness was ~10 km in the west (Armstrong, 1968; Stewart, 1970). Facies changes, sediment

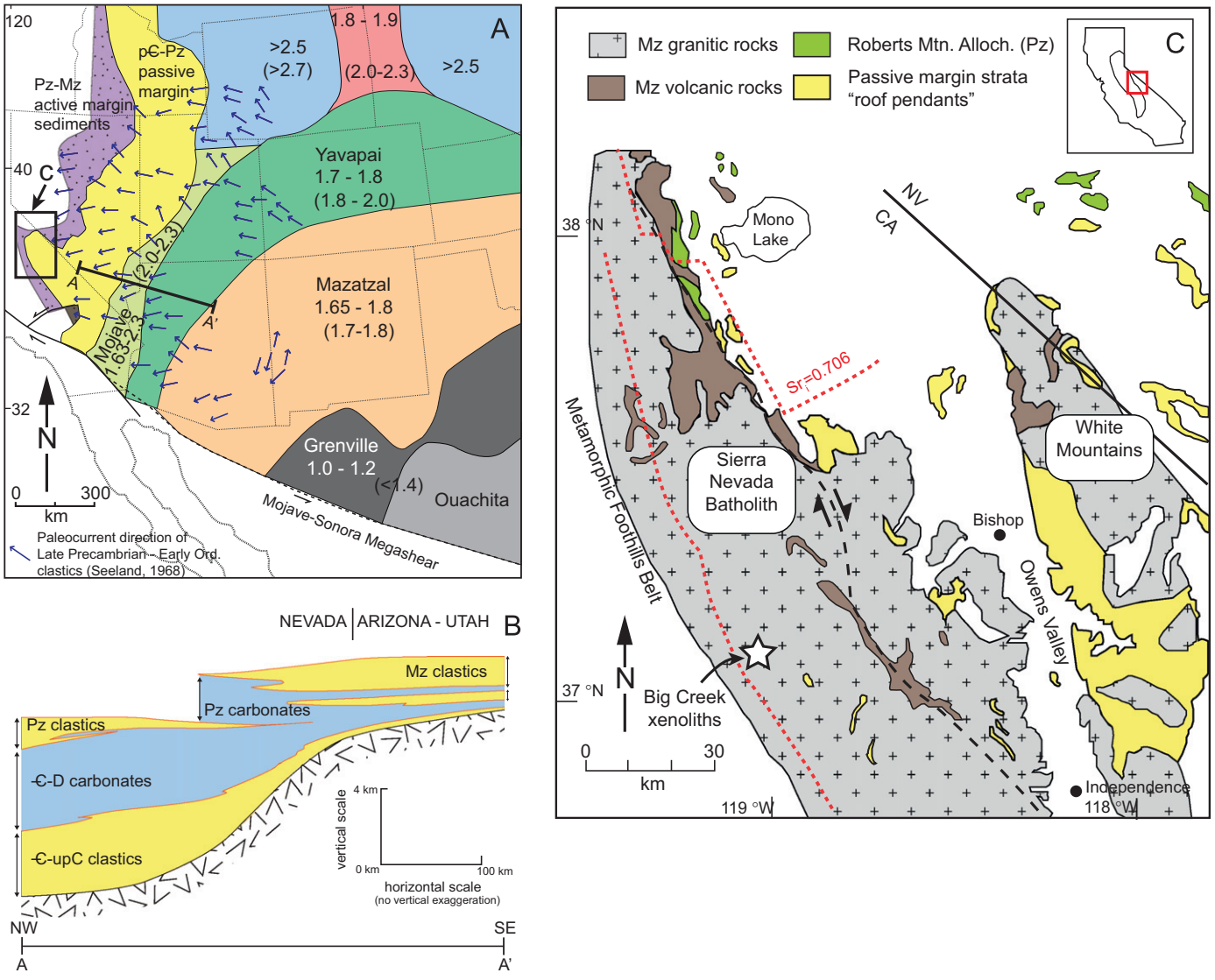

Fig. 1. (A) Map of the Western US, showing the major basement terranes. U–Pb crystallization ages and Hf model ages (parenthesized) are shown. Blue arrows denote paleocurrent directions of Late Precambrian to Early Ordovician clastic sediments and deposition onto the Cordilleran passive margin. (B) Schematic cartoon, modified after Suppe (1985) showing the westward thickening clastic wedge of the Cordilleran miogeocline (passive margin). Sedimentary thickness reached a maximum of ~10 km at the westernmost limit in western Nevada/eastern California. (C) Simplified map of the central–northern Sierra Nevada Batholith. White star represents xenolith locality. Yellow areas represent passive margin rocks now cropping out as roof pendants. (For interpretation of the references to color in this figure legend, the reader is referred to the web version of this article.)

thickness, and paleocurrent directions indicate that the primary direction of sediment transport and deposition was from east to west (Seeland, 1968; Suppe, 1985). Dating of detrital zircons in the passive margin strata indicate provenances of Precambrian North American basement terranes (Bennett and DePaolo, 1987; Gehrels et al., 1995; Grasse et al., 2001) (Fig. 1).

Passive margin deposition ceased when the Farallon plate began subducting beneath western North America in the early Mesozoic, leading to accretion of island arcs and associated juvenile sediments. Cordilleran arc magmatism occurred between 220 and 80 Ma (Chen and Moore, 1982; Stern et al., 1981), resulting in the development of the Sierra Nevada Batholith (SNB). The greatest volume of magma, however, appears to have been emplaced between ~120 and 80 Ma with a pronounced peak in the east-central Sierra between 98 and 86 Ma (Coleman and Glazner, 1997). Plutons associated with arc magmatism were emplaced through the edge of the old passive margin. The paleoboundary separating the ancient passive margin, marking the ancient edge of North America prior to intrusion by Cretaceous granitoids, is inferred from the initial $^{87}Sr/^{86}Sr$ contour of 0.706 in the plutons as defined by Kistler and Peterman (1973) and Kistler (1990). West of this contour, plutons intruded into predominantly Paleozoic and younger accreted terranes; east of this contour, plutons intruded into passive margin strata and presumably ancient North American lithosphere. Relics of these pre-batholithic rocks are preserved as "roof pendants" scattered throughout the SNB, many showing evidence for extensive contact metamorphism.

The focus of this study is a suite of garnet-bearing metasedimentary xenoliths from the Miocene Big Creek diatreme (37° 13′N, 119° 16′W) located in the central SNB. Big Creek is one of the few volcanic pipes within the SNB containing xenoliths sampling all levels of the arc crust and mantle lithosphere. Lower crustal pyroxenite cumulates are most abundant, followed by upper mantle peridotites, granulites, and rare metasedimentary xenoliths. Several studies on the pyroxenites and peridotites have illuminated the nature and evolution of the deep Sierran lithosphere (Dodge et al., 1988; Ducea and Saleeby, 1996; Lee et al., 2000, 2001, 2006; Mukhopadhyay and Manton, 1994).

Due to their rarity, comparably less is known about the metasedimentary xenoliths and their relationship to the crustal architecture of the Sierran arc. Dodge et al. (1988) reported one eclogite-facies, grossular-clinopyroxene xenolith (grospydite) out of a suite of 16 samples, and interpreted the protolith to be a Precambrian carbonate sediment. A more recent study by Ducea and Saleeby (1998) dated one eclogite-facies garnet-bearing quartzite, and obtained a Sm–Nd age of 85.7 ± 3.2 Ma. A study of 23 lower crustal metasedimentary xenoliths from the Eastern Mojave Desert by Hanchar et al. (1994) indicates a heterogeneous lower crust, encompassing the entire spectrum from quartzofeldspathic, pelitic, and mafic lithologies. Two xenoliths from their study are garnet-bearing quartzites similar to the few that have been found in Sierran xenolith suites.

3. Methods

Whole rock major element data were determined by X-ray fluorescence spectroscopy (XRF) at Washington State University Pullman. All samples were sent as whole rocks, ground in-house and fused into di-lithium tetraborate glasses at WSU Pullman. We then determined whole rock trace element geochemistry using the fused glasses by laser ablation ICP-MS (ThermoFinnigan ELEMENT2 with a New Wave 213 nm laser ablation system) at Rice University. The laser was operated with a 110 μm diameter spot size, a ~17 J/cm^2 fluence, and a 10 Hz pulse frequency. Cs, Pb, U, Th, Ba, Rb, Nb, Ta, Y, REE were analyzed in low mass resolution ($m/\Delta m = 300$) and Na, Mg, Al, Si, P, K, Ca, Sc, Ti, V, Cr, Mn, Fe, Co, Ni, Cu, Zn, Ga, Y, and Zr were analyzed in medium mass resolution ($m/\Delta m = 3000$). To ensure reliability of using the glasses, we measured one granulite sample by solution ICPMS and by laser ablation ICP-MS of the fused disks; comparison between the two methods is shown in the Supplemental Information.

Trace element concentrations of minerals (plagioclase, garnet, quartz) were also acquired using LA-ICPMS at Rice University. Polished 200 μm thin sections were analyzed. Depending on mineral grain size, laser spot sizes ranged from 55 to 110 μm. For quartz analyses, we adjusted the operating parameters to 50–80 μm spot sizes and a fluence of 9 J/cm^2, and adjusted the laser frequency to 20 Hz depending on signal intensity. Care was taken to avoid rutile needles present in quartz in both EPMA and LA-ICPMS analyses by checking BSE images and/or examining quartz grains optically prior to measurement. ^{30}Si (for quartz and plagioclase) and ^{25}Mg (for garnet) were used as internal standards to correct for instrumental drift. USGS basaltic glass standards BHVO2g, BIR1g, BCR2g, and the NIST612 glass were used for external calibration, following recommended values given in GEOREM. Sensitivity of the instrument ranged from 180,000 to 250,000 cps per 15 ppm La in BHVO2g for a 55 μm spot operated at 10 Hz and 9 J/cm^2.

Major element concentrations of minerals were determined using wavelength dispersive spectroscopy (WDS) on the CAMECA SX 50 electron microprobe at Texas A&M University. Polished 30 μm thin sections were analyzed. Garnet, quartz, and feldspar standards were used. Spot size was 1 μm, accelerating voltage 15 kV, and probe current 10–20 nA. Probe current was increased to 300 nA to measure titanium concentrations in quartz. For these measurements, we used the Charles M. Taylor pure rutile standard and a pure quartz standard as a baseline check. We used the trace element routine within the CAMECA software to analyze for trace Ti in quartz, and assumed stoichiometric quartz for matrix correction purposes. Due to the extensive decomposition/alteration of the plagioclase, plagioclase grains were imaged in BSE prior to WDS analyses to insure that only unaltered areas were analyzed.

U–Pb and Hf isotopes of detrital zircons were collected simultaneously using a laser ablation system (Photon Machines *Analyte 193H*) attached to a single collector ICP-MS (Thermo-Scientific *Element XR*) and a multi collector ICP-MS (Thermo-Scientific *Neptune Plus*) at UC Davis. After the sample is ablated, the aerosol leaves the sample cell of the laser ablation system and is split into two paths (Tollstrup et al., 2012; Xie et al., 2008), one to the ELEMENT XR for U–Pb isotopes and the second to the Neptune Plus for Hf isotopes. Detrital zircons were measured in situ directly from polished 300 μm thick sections. Due to the small size of most zircons, typical spot sizes used were 30–50 μm. Total data acquisition time was 76 s, with 25–30 s of background acquisition prior to firing the laser, followed by 46–51 s of sample acquisition during ablation. A total of 350 scans of data were acquired during the 76 s integration window, corresponding to ~0.21 s for each individual data point. Zircon standards 91500 (Wiedenbeck et al., 1995), GJ-1 (Jackson et al., 2004), Plesovice (Slama et al., 2008), Temora (Black et al., 2003), and B266 (Stern and Amelin, 2003) were measured prior to and after a set of 5 unknown zircons. Due to the complex zonation of almost all measured unknown zircons, the following data reduction strategy was employed (see Supplemental Online Information for the spreadsheet program).

For U–Pb isotopes, we first subtract average background intensities from the sample intensities. Next, background-corrected ratios of intensities ($^{206}Pb/^{238}U$, $^{207}Pb/^{238}U$, etc.) were calculated. These ratios are then corrected for downhole fractionation (drift) of Pb/U

as laser ablation proceeds through the target grains of sample and standard. We used the exact spot size and laser energy for all analyses within a single standard-sample bracketed analytical session to ensure downhole fractionation of Pb/U observed for standards are applicable to unknown samples. The downhole fractionation of Pb/U was linear with time for all standards with homogeneous composition. The slope of relative Pb/U fractionation with time was thus constant to within error. This slope was defined as $dF/dt = \Delta R/(R_0 t)$, where ΔR is the change in the ratio over time t since initiation of the ablation signal and R_0 is the ratio at the initiation of ablation. Downhole relative fractionation rates (dF/dt) for $^{206}Pb/^{238}U$ (that for $^{207}Pb/^{235}U$ was assumed to be the same) for each zircon standard were identical to within error. These relative fractionation rates were used to correct the time-resolved data of all unknown zircons back to a common baseline, which we took to be the initiation of the ablation signal. This was done using the following equation: $R_t = R_0 + (dF/dt)R_0 t$ where R_t is the ratio measured at time t, R_0 is the ratio drift-corrected back to initiation of the ablation signal, and t is the time elapsed since initiation of ablation. After correction for drift, isotopic ratios are then corrected for instrumental mass bias by normalizing to zircon standard 91500 to obtain the final background-, drift-, and mass bias-corrected ratios. For further details see Tollstrup et al. (2012).

After all corrections were made for every single laser pulse and each individual measurement (scan), we calculated uncertainties by two approaches: counting statistics on the raw data and running average of every 5 corrected data points. In the former method, we calculate the total number of counts (N) on each mass at each time slice using the equation $N = It_d$, where I is the intensity in counts/s and t_d is the total dwell time. The dwell time was 0.01 s for ^{204}Pb, ^{206}Pb, ^{208}Pb, ^{232}Th, and ^{238}U and 0.02 s for ^{207}Pb. The mass window was 3% and we measured 100 samples per peak, thus yielding 3 slices per integration window. We then calculated relative standard error (RSE) using the equation $1/\sqrt{N}$ and then propagated the error on the ratios $^{206}Pb/^{238}U$, $^{207}Pb/^{235}U$, and $^{207}Pb/^{206}Pb$. Percent errors (2RSE) were put into ISOPLOT (Ludwig, 2003) to calculate error ellipses. In the running average method, we continuously averaged every 5 corrected measurements and calculated relative standard errors for each running average. For the counting statistics method, percent errors (1RSE) were put into ISOPLOT to calculate error ellipses. Overall, counting statistics gave lower uncertainties; the difference between the uncertainty from running averages vs. counting statistics generally did not exceed 10%. For comparison, Tollstrup et al. (2012) binned every five scans and calculated the average and associated uncertainties. In this study, we report the uncertainties calculated using counting statistics.

In some samples, the data did not define a clear discordant array, but defined instead a cluster of points. For these zircons, three separate ages were calculated: the $^{206}Pb/^{238}U$ age, the $^{207}Pb/^{235}U$ age, and the $^{207}Pb/^{206}Pb$ age.

Background-corrected Hf isotopes (background correction is done automatically by the Neptune software) were further corrected for instrumental mass bias (assuming exponential mass bias correction) and isobaric interferences of ^{176}Yb and ^{176}Lu on ^{176}Hf off-line using an Excel program written by Tollstrup et al. (2012).

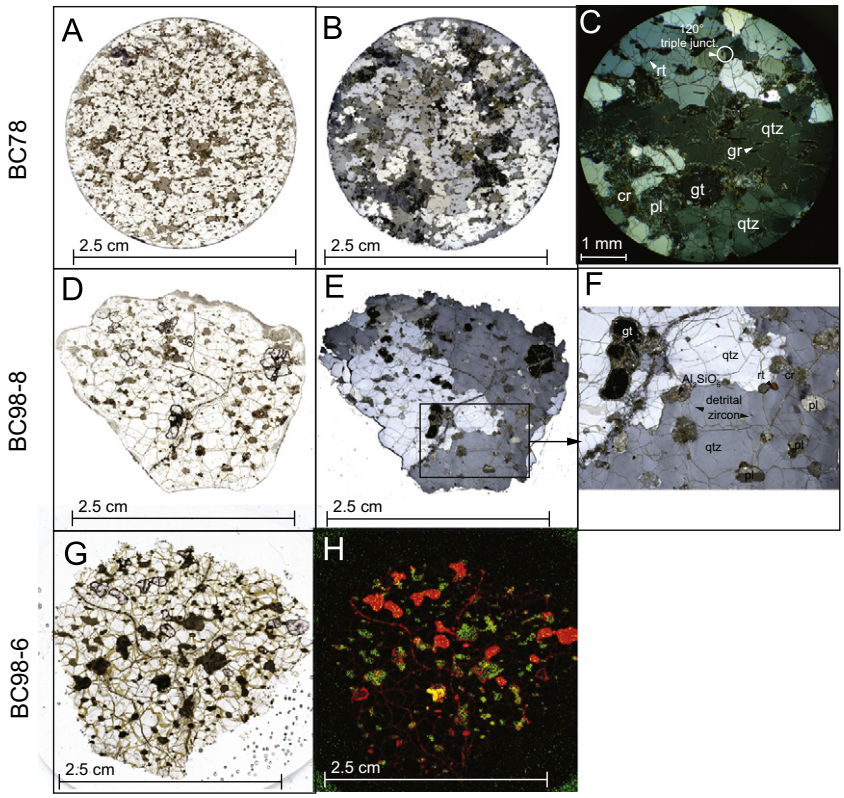

Fig. 2. Petrography of Sierran quartzite xenoliths. (A) Plane-polarized light photograph of thin section (30 μm) of BC78. (B) Same section in (A), but under crossed-nichols. (C) Microphotograph of BC78 (crossed nichols) showing large deformed quartz grains with undulatory extinction at lower right, serrated quartz–quartz contacts, occasional 120° triple junctions, and pervasive melt/fluid infiltration around garnet and through cracks in quartz. Note the decomposition of plagioclase into cryptocrystalline clots. Abbreviations: rt: rutile, gr: graphite, qtz: quartz, pl: plagioclase, cr: cryptocrystalline phase. (D) Plane-polarized light photograph of thin section (30 μm) of BC98-8. (E) Same section in (D), but under crossed-nichols. Note the very coarse size of optically continuous quartz grains (> 1 cm) which all contain undulose extinction. (F) Zoomed-in view of area outlined in (E), showing large garnet porphyroblast and surrounding melt infiltration trails, aluminosilicate grain mantled by altered material, plagioclase (pl) with relict twins, and detrital rutile (rt) and zircon. (G) Thick section (~200 μm) of BC98-6, showing opaque, decrepitated plagioclase blebs, garnet porphyroblasts, and quartz matrix. (H) Micro-XRF map of thick section in (G), where red = Fe, green = Ca and Al. Red areas correspond to garnets and green areas to plagioclase. Red trails are most likely late-stage melt infiltration, possibly from the host magma. (For interpretation of the references to color in this figure legend, the reader is referred to the web version of this article.)

4. Results

4.1. Xenolith petrography

The Big Creek metasedimentary xenoliths (hereafter referred to as "quartzites") are characterized by high quartz content ($>50\%$ by mode), equigranular textures and the presence of large garnet grains ($\sim$1 mm). We focus on four quartzites, BC98-8, BC98-6, BC78, BC134. Approximate mineral modes were determined by point counting ($\sim$1000 points) and/or by least squares inversion of mineral EPMA data and bulk rock chemistry when the appropriate data were available.

BC98-8, BC98-6, and BC78 consist of 60–75% quartz, 8–12% garnet, and 11–30% feldspar. Other phases include $\leq 1\%$ of biotite, trace amounts of orthopyroxene and aluminosilicate, as well as accessory minerals such as graphite, rutile, zircon, apatite, and monazite. BC134 consists of $\sim$20% clinopyroxene, 50% quartz, 30% feldspar. The presence of clinopyroxene and absence of garnet make BC134 distinct. We refer to the former group as the garnet quartzites and the latter as a clinopyroxene quartzite. Because the mineral assemblage in the clinopyroxene quartzite is not diverse enough to provide good constraints on temperature and pressure, we did not analyze BC134 in detail.

Garnet quartzites show signs of late-stage disruption by the host magma and extensive decomposition of feldspars into clays, probably due to post-eruption weathering. Nearly all feldspars have been decrepitated into symplectic, cryptocrystalline intergrowths of clay and relict feldspar. Fluid or melt infiltration is limited mainly to grain boundaries and cracks, with most garnet cores and quartz grains generally clean. Garnet rims contain ubiquitous fine-grained, opaque kelyphites, presumably associated with rapid decompression or localized reaction with infiltrating fluids/melts from the host magma during eruption.

Overall, the quartzites are medium to coarse-grained equigranular and non-foliated, (3 mm–1 cm) (Fig. 2) approaching a granoblastic fabric. Quartz grain sizes of $\sim$1 cm or more are observed in BC98-8, wherein two large, optically continuous quartz grains comprise nearly the entire thin section (2.5 cm), engulfing smaller garnet and plagioclase grains. Such large grain sizes might be evidence for progressive grain growth at high temperatures in the absence of significant deviatoric stresses. Grain boundaries are represented by a spectrum of contact relationships, ranging from serrated quartz–quartz contacts to 120° triple junctions (Fig. 2A–C), the former suggesting grain boundary migration recrystallization (Jessell, 1987; Shelley, 1993) and the latter suggesting evolution towards complete textural equilibration.

In all xenoliths, undulose extinction and subgrain domains are common in quartz. A weak crystallographic preferred orientation may be present based on a qualitative observation of orientation families in quartz. Plagioclase appears as subordinate ovoid blebs engulfed within the larger quartz grains. Garnet occurs as isolated round porphyroblasts. Well-rounded zircons (30–100 μm) are scattered randomly throughout quartz (also as inclusions in garnet). The sphericity and zoning of cathodoluminescence in the zircons suggest a detrital origin (Fig. 3). The zircons have highly luminescent cores, mantled by less luminescent rims. The high luminescence is generally indicative of a former magmatic origin, whereas low luminescence is typical of metamorphic overgrowths. Some detrital cores contain non-luminescent spots and patches, which may be indicative of partial recrystallization at high temperatures (Vavra et al., 1996). Collectively, grain morphology, particularly the high sphericity, and cathodoluminescent features described above suggest a

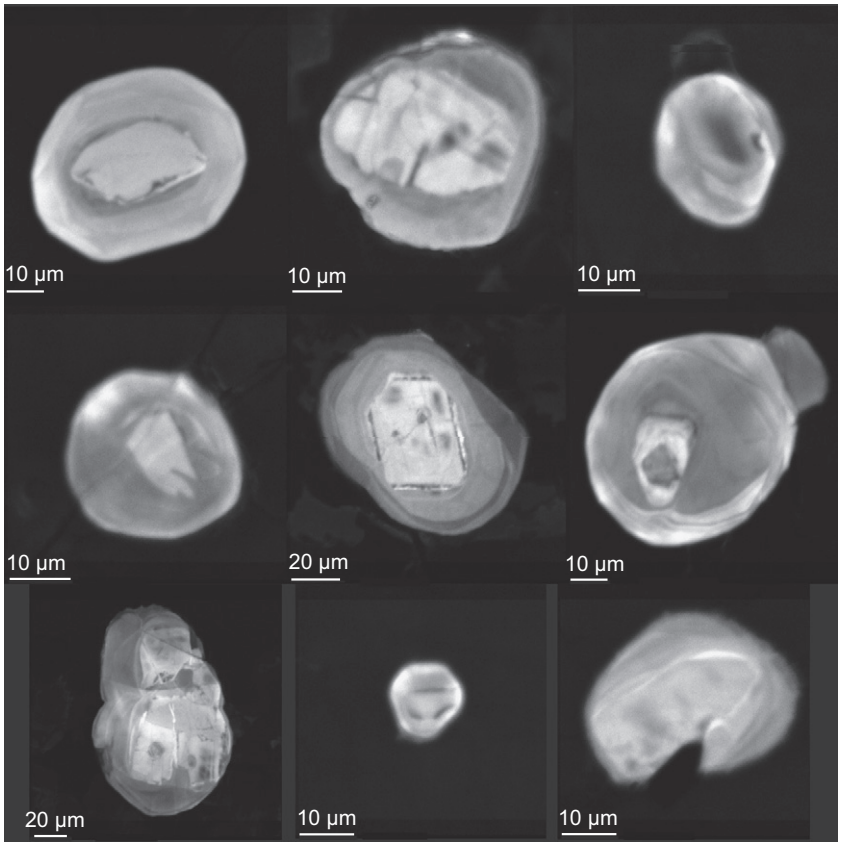

Fig. 3. Cathodoluminescence images of detrital zircons. Detrital cores are bright and luminescent, some cores have spongy textures and patches, which may be a result of high-temperature partial recrystallization. Detrital cores are rimmed by metamorphic overgrowths, the contact between core and overgrowth is often dark, grading into more luminescent.

metamorphic history characterized by residence of the zircons at elevated temperatures followed by new zircon growth. High initial Zr concentrations in the protoliths (> 100 ppm) may have provided the source for dissolution–reprecipitation reactions responsible for large metamorphic overgrowths (Rubatto et al., 2001), and prolonged residence at high temperatures (where Zr solubility is high; (Watson and Harrison, 1983)) may have facilitated Ostwald ripening as a mechanism of overgrowth (Nemchin et al., 2001).

4.2. Whole rock geochemistry

4.2.1. Major element systematics

Whole-rock major element compositions are reported in Table 1 (Supplemental Online Information). Binary oxide variation diagrams are shown in Fig. 4A–D. All quartzites are characterized by high SiO_2 (> 80 wt%) and low Al_2O_3 (< 6 wt%) compared to average upper continental crust, which has 66 wt% SiO_2 and 15 wt% Al_2O_3 (Rudnick and Fountain, 1995). The quartzites are also depleted in K_2O (< 1 wt%) compared to upper continental crust which has 3 wt% K_2O. In Fig. 4, we also show for comparison passive margin siliciclastic rocks from the Great Basin to eastern California (Stewart, 1970). These rocks are now represented by roof pendants within the Sierra Nevada Batholith, although some units are also well exposed east of the Sierra in the White and Inyo Mountains. Compositions from the nearby Boyden Cave roof pendant (Girty et al., 1994) as well as metapelitic wallrocks from Southern Sierra Nevada roof pendants and leucosomes derived therefrom (Zeng, 2004) are also shown. Finally, we also include a suite of calc-silicate wallrocks from the Peninsular Ranges Batholith (Morton, unpublished data). All of these rocks, based on proximity and compositional similarities, represent possible protoliths of the Sierran quartzites.

In binary plots of Al_2O_3, K_2O, and MgO + FeO vs. SiO_2 (Fig. 4A–C), the metasediments and the xenoliths show negative trends corresponding to decreasing amounts of feldspar, mica, and mafic minerals with increasing quartz content, which are features of increasing sediment maturity. The Sierran garnet quartzite xenoliths, which plot on the quartz-rich end of the array, clearly derive from quartz-rich protoliths and not more aluminous (pelitic) protoliths. In Fig. 4D, we also plot CaO vs. SiO_2 along with binary mixing arrays between pure calcite and an end-member varying

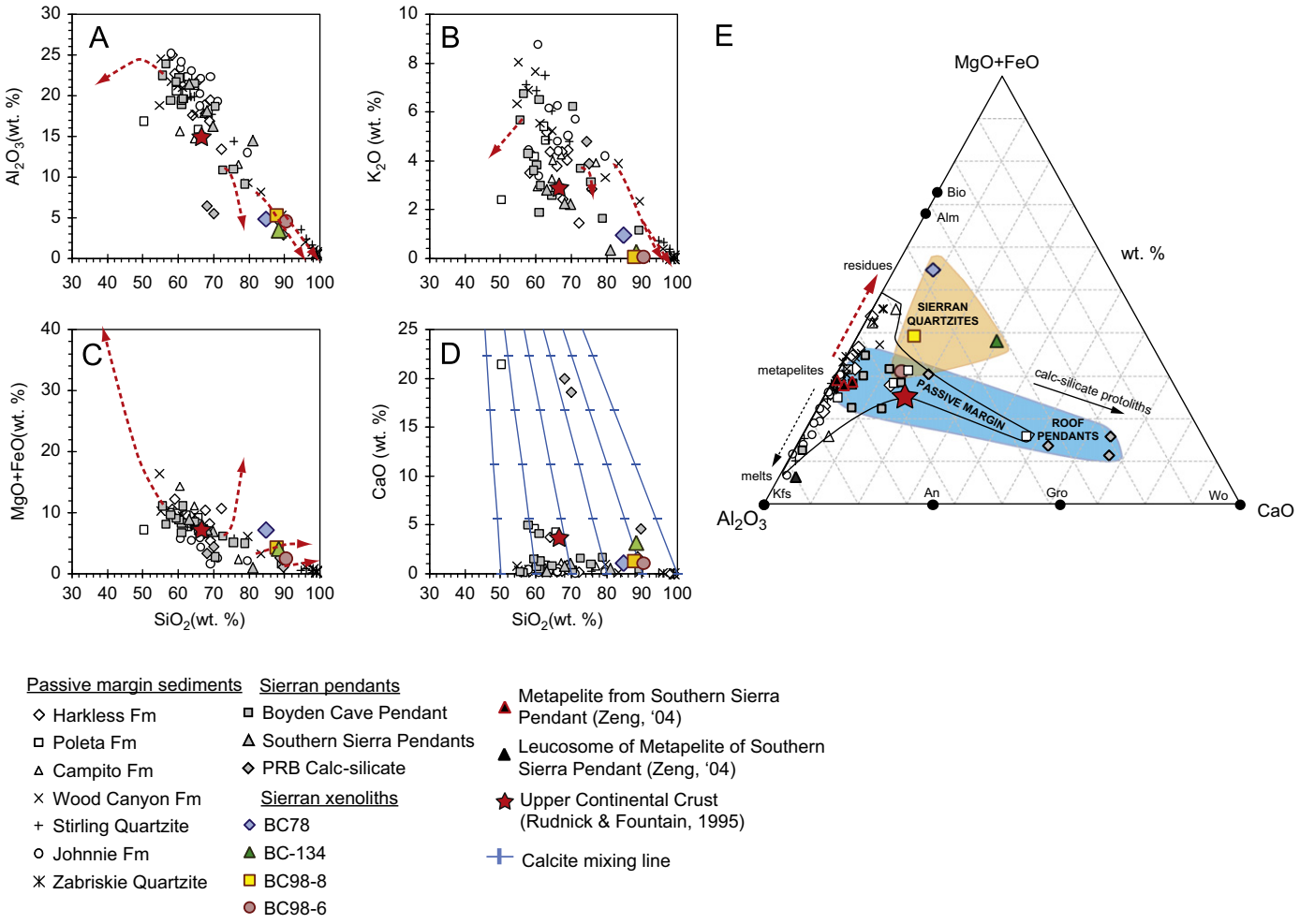

Fig. 4. Major element systematics of Sierran quartzites and related rocks. Open symbols represent passive margin sediments of the western Great Basin and eastern California (Stewart, 1970), filled grey symbols represent Sierran roof pendants (Girty et al., 1994) and calc-silicate wallrocks from the neighboring Peninsular Ranges Batholith (Morton, unpublished data), filled colored symbols represent Sierran quartzite xenoliths. (A) Al_2O_3 vs. SiO_2, (B) K_2O vs. SiO_2, (C) FeO + MgO vs. SiO_2 (FeO is reported as FeOT), (D) CaO vs. SiO_2. Thick red dashed lines represent trend of partial melting residues for 4 protoliths starting with different SiO_2 contents (see text); note that residues of partial melting increase in Si only if the protolith is already silica rich, e.g., SiO_2 > 70 wt. %. Blue lines with tick marks represent binary mixing lines with pure $CaCO_3$ mixed with an end-member varying from pure SiO_2 to 50 wt% SiO_2. (E) Ternary plot in wt% of MgO + FeO, Al_2O_3, and CaO. Black triangles with red outline are three metapelitic wallrocks from the Southern Sierra analyzed by Zeng (2004) and their corresponding leucosome (black triangle). Thin black dashed line shows a schematic vector of melts derived from metapelites; thick red dashed lines show complementary residues (schematic). Red star represents upper continental crust composition from Rudnick and Fountain (1995). (For interpretation of the references to color in this figure legend, the reader is referred to the web version of this article.)

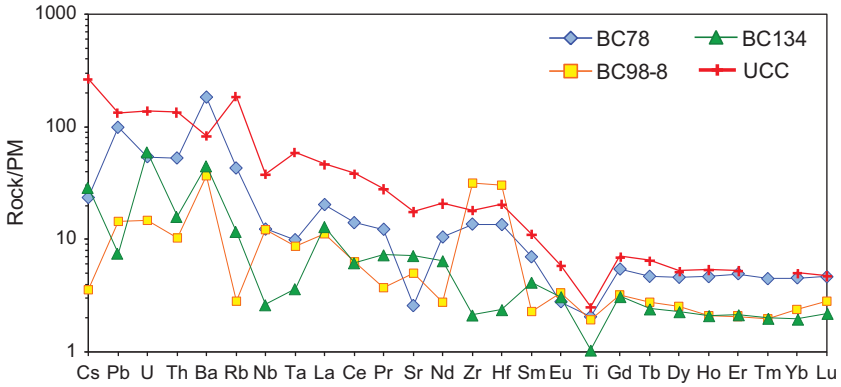

Fig. 5. Whole-rock primitive-mantle normalized trace element spidergrams of Sierran quartzites. Upper continental crust from Rudnick and Fountain (1995) is shown for reference.

from pure quartz to 50 wt% quartz in order to assess the extent to which the protolith may have contained carbonate. All the garnet quartzite xenoliths and most of the siliciclastic roof pendants are highly depleted in CaO and show no correlation between CaO and SiO_2. However, a few roof pendant suites and the Peninsular Ranges wallrocks are enriched in CaO, suggesting mixing with calcite. The clinopyroxene quartzite, BC134, has higher CaO (3 wt%) compared to the other xenoliths, suggesting a calcareous quartzite as a protolith. Fig. 4E shows a ternary plot of MgO+FeO, Al_2O_3, and CaO, which provides some additional insights to binary diagrams. The Sierran quartzites do not fall within the fields bounded by passive margin sediments or their metamorphic analogs, the Sierran roof pendants. The quartzites trend towards higher FeO and MgO contents, an observation also borne out by the steeper array on a binary plot of FeO+MgO vs. SiO_2 (Fig. 4C), compared to passive margin and roof pendant rocks. In a later section, we discuss whether these trends may be the result of partial melting.

4.2.2. Trace element geochemistry

Whole rock trace element geochemistry is reported in Table 2 (Supplemental Online Information) and primitive mantle-normalized (McDonough and Sun, 1995) trace element abundance diagrams are shown in Fig. 5. Average upper continental crust (UCC) of Rudnick and Fountain (1995) is also shown for comparison. The rare-earth element (REE) abundance patterns show relative enrichment in light REEs relative to the heavy REEs and are generally similar in shape to UCC and Sierran metasandstones from the nearby Boyden Cave roof pendant (Girty et al., 1994), a potential protolith. However, in absolute abundance, they are depleted in REEs. This depletion in REEs correlates negatively with SiO_2 and positively with Al_2O_3, indicating that the depletion in REEs is related to dilution by quartz content. Zr and Hf concentrations are highly variable as shown by the positive and negative depletions relative to Sm and Nd in normalized abundance diagrams. This variability is likely controlled by the abundance of zircon, as exemplified by the fact that BC98-8 has the most positive Zr–Hf anomaly and the highest observed zircon abundance. In contrast, BC134, which lacks zircon altogether, has a negative Zr–Hf anomaly.

4.3. Mineral chemistry

4.3.1. Major elements (garnet and feldspar)

Major element compositions of garnet and clean, relict plagioclase are reported in Table 3 (Supplemental Online Information). Garnets are overall unzoned, although rims are slightly Ca-enriched (4 wt% vs. 3.5 wt% in cores). Almost all garnet rims have been altered by contact with infiltrates of the host basaltic melt, thus the observed Ca zonation is most likely not an inherent feature of the garnet. Average end-member compositions of all garnets in the two samples analyzed (BC98-8, BC78) are nearly identical at $Gr_{10}Py_{40}Al_{50}Sp_{0.8}$. Mg♯ of garnets are between 42 and 48.

Although most feldspars decomposed or were altered to clays and cryptocrystalline phases, we were able to find areas that still preserved relict compositions by screening with back-scattered electron imaging and checking the compositions using energy-disperse wavelength (EDS) spectroscopy. BC98-8 contained only plagioclase and no alkali feldspar (average end-member composition $Ab_{72}Or_2An_{26}$). BC78 contained mostly plagioclase (average $Ab_{47}Or_5An_{48}$) with minor alkali feldspar. In most cases, it was difficult or impossible to obtain rim–core traverses due to the degree of alteration, so we analyzed 3–4 spots throughout individual grains to determine if compositional variability was present. In general, plagioclases were unzoned.

4.3.2. Trace elements (garnet, plagioclase, quartz)

Trace element compositions of garnet, feldspar, and quartz are reported in Tables 4 and 5 (Supplemental Online Information). Garnet cores in BC98-8 contain higher HREE abundances than corresponding rims, which might be related to growth zoning. No variation in HREE composition was observed in garnet in BC78. An interesting feature of both garnet and plagioclase is that, within a given sample, both minerals show complementary Eu anomalies (garnet a negative Eu anomaly and plagioclase a positive Eu anomaly). The complementary Eu anomaly in garnet and plagioclase indicates that garnet equilibrated with plagioclase. Average ($n=23$) Ti concentrations in quartz for BC78 is 165 ppm; average Ti is 85 ppm for BC98-8, and average Ti for BC134 is 44 ppm.

4.4. U–Pb and Hf isotope geochemistry

Lu–Hf and U–Pb isotopic data for zircons are reported in Table 6 (Supplemental Online Information). In Fig. 6, we show 6 representative detrital zircon analyses. Each individual panel of the figure corresponds to one zircon grain, and each error ellipse corresponds to one measurement from a single laser pulse. As shown in Fig. 6, the zircons are all discordant with variable but ancient (>1 Ga) upper intercept ages, but a common lower intercept age centered around a weighted mean of 103 ± 10 Ma (2σ) (Fig. 7). We interpret the discordia to represent a mixture line between old detrital cores (upper intercept) and a younger metamorphic overgrowth (lower intercept).

In Fig. 8, we plot εHf values vs. age for the zircons. Despite having two distinct U–Pb isotopic signatures corresponding to an upper and lower intercept age, Hf isotopes were homogeneous within individual zircon grains. For each zircon, we plot εHf_i, using the upper intercept age, and "εHf_0", using the lower intercept age. Colored arrows are

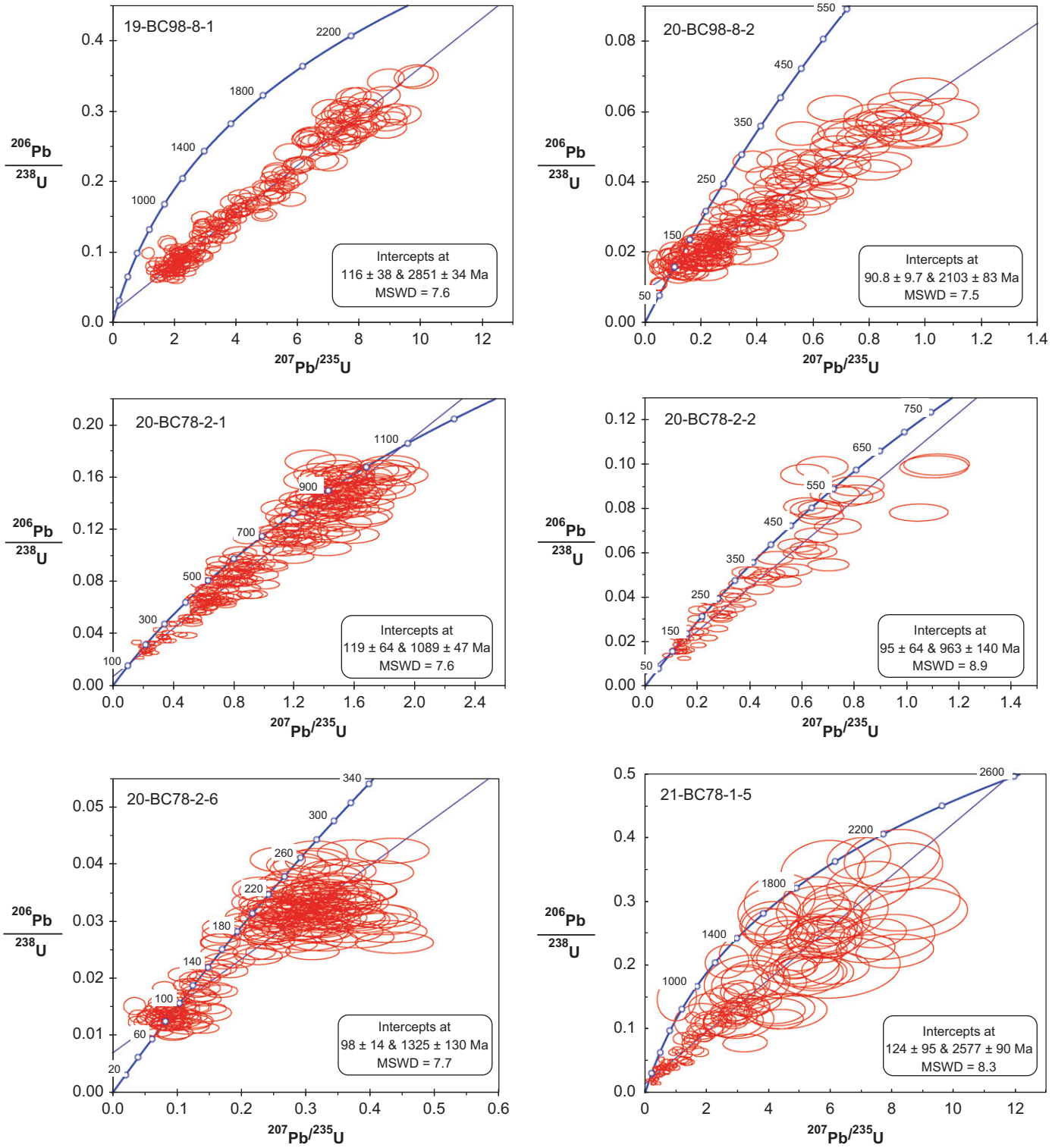

Fig. 6. Representative U–Pb concordia diagrams showing typical discordia of detrital zircons. Each panel represents one zircon (> 200 individual measurements per analysis). Data point ellipses are 2σ as calculated by Isoplot. Uncertainties reported do not include uncertainty on the decay constants of ^{238}U and ^{235}U.

drawn to schematically connect the detrital zircon core (εHf_i) to corresponding metamorphic overgrowth rims (εHf_0). The following values were used in calculating εHf and plotting the depleted mantle evolution line: $(^{176}Hf/^{177}Hf)_{CHUR,present}=0.282785$ and $(^{176}Lu/^{177}Hf)_{CHUR,present}=0.0336$ (Bouvier et al., 2008); $(^{176}Lu/^{177}Hf)_{DM,present}=0.03933$ and $(^{176}Hf/^{177}Hf)_{DM,present}=0.283294$ (Vervoort and Blichert-Toft, 1999).

5. Final *P–T* conditions

5.1. Titanium-in-quartz and garnet–aluminosilicate–quartz–plagioclase geothermobarometry

To place constraints on the pressure and temperature conditions at which the quartzites last equilibrated, we combined

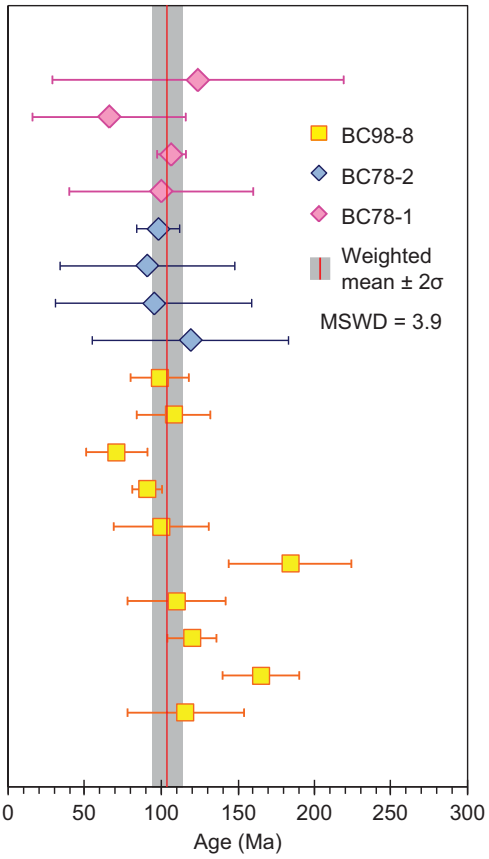

Fig. 7. Plot of lower intercept ages (Ma) of individual zircon grains (symbols correspond to host xenolith; each point=one zircon grain). Black line represents weighted mean of lower intercepts at 103 ± 10 Ma, grey band represents uncertainty (2σ) on the weighted mean.

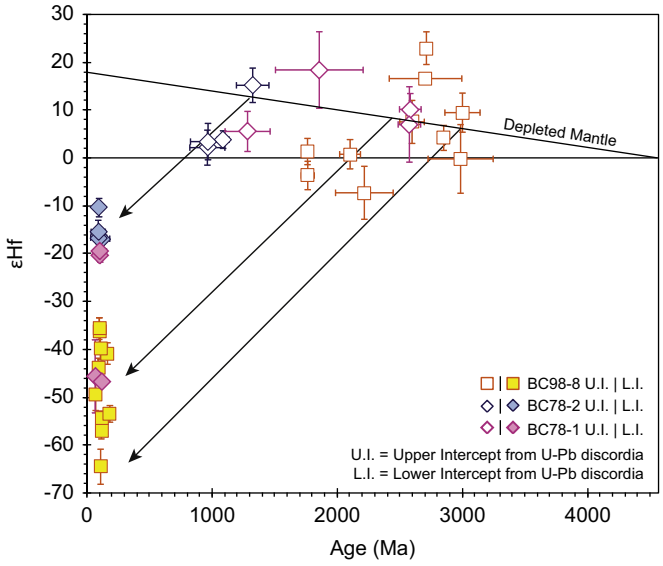

Fig. 8. εHf vs. age (Ma) of zircons. Each zircon grain is represented by two points on the diagram—the open outlined point corresponds to the upper intercept age, the colored outlined point corresponds to the lower intercept age determined from U–Pb discordia. Black arrows are schematic and illustrate initial zircon crystallization and subsequent isotopic evolution (note that the zircons' $^{176}Hf/^{177}Hf$ ratio does not change as evidenced by the homogeneous values obtained for individual zircon grains; rather the evolution towards very negative εHf values is largely driven by the growth of the CHUR reservoir from 2 Ga to 100 Ma). (For interpretation of the references to color in this figure legend, the reader is referred to the web version of this article.)

geothermobarometry and thermodynamic modeling. Rutile coexists with quartz in all samples, simplifying activity relations so that $a\mathrm{TiO_2}$ in rutile=1 and thus the equilibrium constant $K \sim a\mathrm{TiO_2}$ in quartz when using the titanium-in-quartz geothermometer (Wark and Watson, 2006). Ti-based temperatures are between 730 and 810 °C for garnet quartzite xenoliths BC98-8 and BC78 (corresponding to the average of 85 and 165 ppm Ti, respectively). Because Ti concentrations measured by EPMA were systematically lower than by LA ICP-MS (EPMA was on average 30–50 ppm less than ICP-MS), EPMA data gave slightly lower temperatures (50–70 °C) than LA ICP-MS data. The discrepancies between Ti measured by LA ICP-MS and EPMA could be related to the larger spot size ($\geq$30 μm) used in laser ablation compared to that used in EPMA (1 μm), resulting in the incorporation of rutile needles into the analysis during laser ablation. If the rutile needles are of exsolution origin, the laser ablation results provide a better measure of the peak metamorphic temperatures, but if they are not of exsolution origin, the EPMA results are likely to be more representative. We are not able to further resolve this issue.

For final pressures of equilibration, we used the "GASP" geobarometer (garnet–aluminosilicate–silica–plagioclase) (Koziol and Newton, 1988; Spear, 1995). Due to the difficulty of obtaining unaltered rim–rim mineral pairs between plagioclase and garnet, we used average mineral compositions (this is justified because the minerals are mostly unzoned). Results are shown in Fig. 9A. For input temperature of 730 °C from Ti-in-quartz temperatures, average albite content of 71% in plagioclase, average grossular content of 9% in garnet, and activities of quartz and aluminosilicate of 1, we obtain a pressure of 1.1 GPa for sample BC98-8. We obtain the same pressure, within error, for sample BC78.

5.2. Stability field of plagioclase+garnet

To further constrain metamorphic *P–T* conditions, we determined the stability field wherein plagioclase and garnet coexist for a given quartzite bulk composition using the software THERIAK DOMINO to calculate equilibrium assemblage diagrams (de Capitani and Petrakakis, 2010). Using sample BC98-8, and considering only Si, Ca, Al, K, Mg, Fe (no H_2O) in the system, we calculated the volume % of stable minerals in the assemblage at fixed T and varying P. We show an isothermal section at 750 °C in Fig. 9B. The plagioclase+garnet stability field spans a wide interval from 0.4 to >1 GPa, but based on the estimated modes in BC98-8, we narrow this window to 0.7–1.0 GPa. The modeled modes of garnet and plagioclase calculated for the range 0.7–1.0 GPa roughly match the observed modes (see sample descriptions). Despite the discrepancies between the model and the actual rock, overall the *P–T* interval in which garnet and plagioclase are stable overlaps the *P–T* interval determined using geothermobarometry.

6. Discussion

6.1. A passive margin origin for the Sierran lower crustal quartzite xenoliths

The Sierran quartzites record last equilibration at lower crustal pressures (0.7–1.0 GPa) and relatively high temperatures (730–810 °C). High temperatures are consistent with the rock textures. Coarsening of quartz grains to >1 cm (Fig. 2), engulfment of plagioclase and garnet by quartz, and the deformed nature of the quartz matrix suggest static and/or dynamic recrystallization of an originally equigranular quartzitic protolith under high temperatures, where diffusivities are high. The recrystallized fabric and significant grain growth could have formed after emplacement into the lower

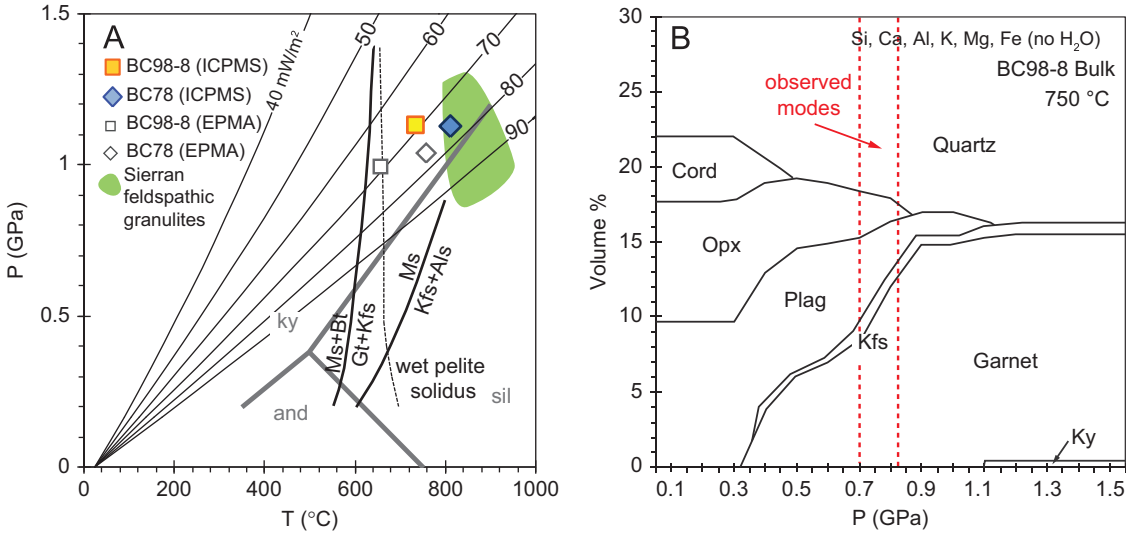

Fig. 9. (A) *P–T* diagram showing the final equilibration conditions of Sierran quartzites. Colored symbols correspond to LA ICP-MS measurements of Ti in quartz (used as input temperatures into the GASP barometer), whereas white symbols refer to EPMA measurements of Ti used as inputs. Green field represents feldspathic granulite xenoliths, shown for comparison, from the same locality measured by Ducea and Saleeby (1996). Thin black curves represent a family of crustal geotherms constrained by surface heat flow ranging from 40 to 90 mW/m^2 (assuming a heat production of 0.7 μW/m^3 (Rudnick et al., 1998) and a 35 km thick crust). Wet pelite solidus and mica dehydration curves are for the model system KNFASH (K, Na, Fe, Al, H_2O and quartz-saturated) and are taken from (Bucher and Frey, 1994). (B) Isothermal P-X diagram at 750 °C, calculated using THERIAK DOMINO (de Capitani and Petrakakis, 2010) for bulk composition of sample BC98-8. Only Si, Ca, Al, K, Mg, and Fe (no H_2O) was modeled. Cord = cordierite, Opx = orthopyroxene, Plag = plagioclase, Kfs = alkali feldspar, Ky = kyanite. (For interpretation of the references to color in this figure legend, the reader is referred to the web version of this article.)

crust if temperatures were high and deviatoric stresses low, thus permitting grain coarsening. Metamorphic overgrowths on detrital zircons, some of which are thick compared to the diameter of the detrital core (Fig. 3), may also have formed via grain coarsening or Ostwald ripening due to sustained high temperatures.

Despite such elevated final *P–T* conditions, the quartzite xenoliths do not resemble typical granulite xenoliths characteristic of the lower crust, which are intermediate (~50 wt% SiO_2) to mafic in composition (Rudnick and Fountain, 1995). Instead, the high bulk SiO_2 contents and correspondingly high quartz modes, combined with the abundance of rounded zircons preserving detrital cores strongly point to a sedimentary origin. The detrital zircon cores yield U–Pb crystallization ages representative of North American basement, indicating that the quartzites' protoliths are mature, siliciclastic sediments of the Proterozoic and Paleozoic passive margin of western North America (Fig. 1), deposited prior to Mesozoic arc magmatism. The U–Pb crystallization ages for the detrital cores overlap those of well-known passive margin rocks of the Salinian Block and Snow Lake Pendant (Barbeau et al., 2005; Grasse et al., 2001), which form part of the sedimentary framework rocks into which the Sierra Nevada batholith intruded. The extremely low εHf_0 values also corroborate the origin of the detrital zircons from Proterozoic crustal reservoirs instead of recently accreted oceanic and juvenile arc terrane sources. Furthermore, the Hf isotope systematics are similar to those of basement underlying the eastern Sierra Nevada batholith (Lackey et al., 2012), which is predominantly composed of ancient North American crust. Thus, the protoliths of the Sierran quartzites are unlikely to be juvenile sediments in the oceanic trench and accretionary complex of the Mesozoic subduction zone.

6.2. Mid-Cretaceous timing of metamorphic overprinting

The timing of metamorphic overprinting can be interpreted using the discordant U–Pb zircon arrays (Fig. 6). The discordant arrays are unlikely to represent continuous Pb loss because the data do not show the curvature expected for continuous Pb loss (Tilton, 1960). The fact that the zircons in almost all of the samples share a common lower intercept of 103 ± 10 Ma, despite having variable detrital core ages, suggests that all of the zircons share a common metamorphic overgrowth, and therefore together experienced a major thermal event at this time. Th/U ratios in zircon overgrowths are generally < 0.2, also consistent with a metamorphic origin (Hoskin and Black, 2000). Intriguingly, this common lower intercept of 103 ± 10 Ma coincides with the average U–Pb zircon crystallization age of 102 Ma of plutons near the xenolith locality (Stern et al., 1981), suggesting that the metamorphic overprint is probably related to a thermal overprint induced by mid-Cretaceous arc magmatism.

6.3. Mechanisms of emplacement

We now consider three possible scenarios by which passive margin sediments could have been transported to lower crustal depths > 20 km and temperatures in excess of 700 °C (Fig. 9): (1) Underthrusting of continental crust beneath the continental arc, (2) viscous return flow of wallrock in response to diapiric rise of plutons, and (3) underplating by buoyant sediment diapirs derived from the subducting Farallon plate.

Hypothesis 1. Continental underthrusting beneath the arc

In the first hypothesis, North American continental lithosphere, loaded with thick Paleozoic and older passive margin sediments, is thrust westward beneath the continental arc (Fig. 10A). The average metamorphic overprint age of 103 ± 10 Ma provides a lower bound on when underthrusting happened. The question is whether underthrusting occurred well before or coevally with mid-Cretaceous arc magmatism.

If underthrusting of these passive margin sediments to lower crustal depths occurred before Cretaceous magmatism, older metamorphic overprints or more complex single-grain zircon U–Pb discordia would be expected, but no such features are seen. The simplicity of the U–Pb systematics (common lower intercept and linear Discordia) within individual zircon grains instead are

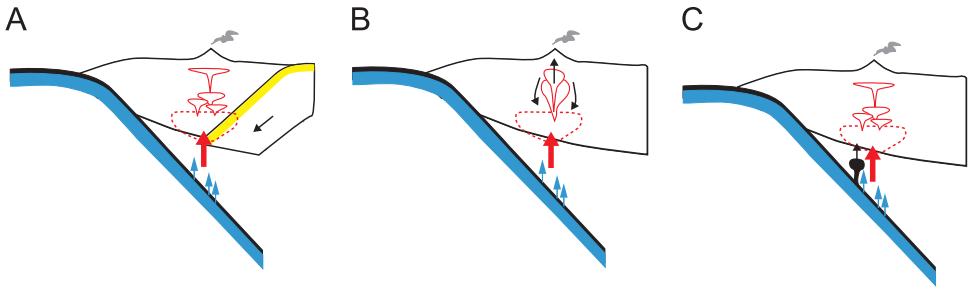

Fig. 10. Cartoons illustrating three scenarios proposed for transport of quartzites into lower crust. Dashed red line represents a hypothetical deep crustal "hot zone" or "MASH" zone associated with arc magmatism. Thick red arrow represents mantle-derived flux of basaltic magma. Thin blue arrows represent devolatization of the slab. (A) Continental underthrusting of upper plate continental lithosphere beneath arc. Passive margin sediments represented by yellow. (B) Return flow of wallrocks during pluton diapirism. (C) Underplating of lower crust by sediment diapirs derived from subducting slab. Black shape represents sediments rising from slab surface. (For interpretation of the references to color in this figure legend, the reader is referred to the web version of this article.)

better explained by one thermal overprint, which suggests that if tectonic underthrusting is a viable hypothesis, underthrusting was likely coeval with Cretaceous arc magmatism. Such a scenario would be consistent with current views on the tectonic history of the region, which we discuss below.

Westward underthrusting of the North American continent is thought to have occurred to balance the eastward transport of upper crustal rocks into the foreland by thin-skinned deformation during the Cretaceous and is now manifested as the Cordilleran fold-and-thrust belts (DeCelles et al., 2009; Oldow et al., 1990). The role of deep, lithospheric-scale underthrusting has been inferred from Nd isotopic shifts in arc magmas resulting from emplacement of old, evolved continental material beneath the arc (Ducea and Barton, 2007). At greater depths within the arc lithosphere, Sierran mantle xenoliths record evidence of downward compression of initially shallow, melt-depleted spinel peridotite residues which were thickened and metamorphosed into garnet lherzolite (Chin et al., 2012). These studies indicate that continental arc lithosphere at all levels records the evidence of tectonic compression and downward transport of shallow material to depth. Underthrusting is thus one possible way in which the Sierran quartzites could have been transported from their shallow origins into the lower crust.

Hypothesis 2. Viscous return flow of wallrocks during pluton ascent

A second hypothesis involves the downward transport of upper crustal rocks by viscous return flow in response to diapiric rise of plutons (Fig. 10B) (Saleeby et al., 2003). This process, however, would have to displace upper crustal sediments (maximum burial depths of 6 km have been inferred by Stewart (1970)) to lower crustal depths, requiring at least 10 km of downward transport. Such extensive downward transport of the quartzites would, however, have to compensate for the very low density of quartzites, which would have generated positive buoyancy opposing the forced downflow. Another issue is that wallrocks are probably highly viscous owing to their felsic composition and cold ambient temperatures compared to ascending and evolving magmas, which are also viscous. Thus, high viscosities are another barrier to wallrock return-flow. Furthermore, pluton ascent is widely thought to occur by diking rather than diapirism (Petford, 1996). Dike ascent does not involve viscous downflow of the country rock.

Hypothesis 3. Underplating by slab-derived sediment diapirs

A third scenario invokes underplating of the continent by buoyant sediment diapirs derived from the downgoing Farallon oceanic plate (Fig. 10C). Recent studies (Behn et al., 2011; Hacker et al., 2011) have proposed that such a process could be important for transporting felsic rocks, aided in part by partial melting of sediments on the subducting oceanic plate, into the lower crust at continental arcs. However, the Proterozoic to Archean provenances of the detrital zircons strongly suggest that the protoliths derive from passive margin sediments on the North American continent. Any sediments derived from the oceanic trench would most likely consist of a large fraction of Mesozoic protoliths, which is not seen in our zircons.

6.4. Possibility of partial melting

The high temperatures of the quartzite xenoliths (700–800 °C) are higher than the wet solidus of granitic rocks, begging the question of whether the quartzites may represent restites of partial melting. Based on our discussions in Section 6.3, our preferred hypothesis for the emplacement of quartzites into the lower crust is that they were underthrusted during the peak of arc magmatism. If so, such melting would have profoundly influenced deep-seated magmas.

To investigate whether the quartzites represent partial melting residues, we performed melting calculations using rhyoliteMELTS (Gualda et al., 2012) on four possible protoliths, chosen to span a range of crustal metasedimentary rocks. Three protoliths are roof pendant rocks from Boyden Cave Pendant (Girty et al., 1994), varying from impure quartzite (90% SiO_2), feldspar-bearing quartzite (73% SiO_2), to pelite (56% SiO_2). The fourth protolith is feldspathic arenite (82% SiO_2) of the Wood Canyon Formation (Stewart, 1970). Full compositional data on the protoliths and melting products are given in the Supplemental Online Information. We modeled partial melting at isobaric conditions (1 GPa) over temperatures between 500 and 1200 °C and fO_2 buffered at quartz–fayalite–magnetite. Water contents in the protoliths were 2% for the impure quartzite and the sandstone, 3% for the feldspar-bearing quartzite, and 4% for the pelite. Details of the inputs and outputs to the modeling are provided in the Supplemental Online Information.

In Fig. 4A–C, we show the residue trends between 500 and 900 °C for the 4 protoliths as dashed red arrows. The most important feature is that protoliths with <70 wt% SiO_2, yield quartz-poor residues, whereas protoliths with >70 wt% SiO_2 yield quartz-rich residues. The kink in Al_2O_3 in the melting residue of the pelite protolith corresponds to exhaustion of micas and a steep increase in residual garnet at 765 °C. In the plot of MgO+FeO vs. SiO_2 (Fig. 4B) the evolution toward garnet-rich residues (>10% garnet by mode) is most pronounced in the pelitic and feldspar-bearing quartzite protoliths (<70 wt% SiO_2), which have the highest initial MgO, FeO and Al_2O_3 contents. By contrast, garnet mode in protoliths with >70% initial SiO_2 evolve <10% modal garnet in their residues. In Fig. 4C, K_2O decreases in

all residues, due to melting out of mica (in pelitic protoliths) or feldspars (in feldspar-bearing quartzite, feldspathic arenite, and impure quartzite).

Based on the model results, the quartzite xenoliths are clearly not residues of partial melting of pelites, which would have too little quartz and too much garnet compared to the xenoliths. Instead, the protoliths of the quartzite xenoliths must initially have had >70 wt% SiO_2. We can further rule out a feldspathic quartzite protolith because residues of this protolith would have $>10\%$ residual garnet, but the observed garnet mode in the quartzite xenoliths is $<12\%$. For these reasons, the protoliths of the xenoliths were most likely impure quartzites. Given that the quartzite xenoliths contain no micas and yet have small amounts of garnet and feldspar, the minimum melting temperature would be 750 °C at 1 GPa. Our model results suggest that if the quartzite xenoliths represent restites, at most 25% melting had occurred because of the relatively infertile nature of quartzite protoliths. Very high temperatures (>1300 °C at 1 GPa) are required to generate more than 50% melt from such an "infertile" protolith (Clemens and Vielzeuf, 1987). For comparison, pelites yield 70% melt at $\sim$750 °C according to our model results. The contrast in fertility between pelites and quartzites has been observed in Alpine settings such as the Trois Seigneurs Massif (Wickham, 1987), where pelites have undergone extensive partial melting and quartzites, under the same conditions remain, unmelted.

In summary, it seems likely that the quartzite xenoliths are the residues of small to moderate degrees of partial melting in the lower crust. Partial melting, to the point of mica exhaustion at pressures of 1 GPa, suggests melting temperatures of 750 °C, which coincidentally is within the range of the Ti-in-quartz thermometry results. Attaining such high temperatures by tectonic underthrusting alone would seem difficult. England and Thompson (1986) showed that rapid crustal thickening results in decreased thermal gradient. An external heat source seems required. One possibility could be the intrusion of mafic magmas into the lower crust, generating deep crustal hot zones (Annen et al., 2006; Hildreth and Moorbath, 1988). As shown in Fig. 9A, crustal geotherms bounded by a range of surface heat flows (40–80 mW/m^2) strongly suggest that heat flow ≥ 70 mW/m^2 is required to explain the temperatures recorded by the Sierran quartzites (as well as other crustal granulite-facies xenoliths from the Sierra Nevada from work by Ducea and Saleeby (1996)). Such high heat flows are characteristic of active continental arcs, such as the modern Andes (Springer and Forster, 1998).

7. Summary and implications

We studied the petrology, geochemistry, and metamorphic history of garnet-bearing quartzite xenoliths sampled in late Miocene basalts erupted through the Sierra Nevada. High quartz mode ($>50\%$) and abundant well-rounded detrital zircons support a sedimentary protolith, such as a mature quartz arenite. Metamorphic garnet, high Ti concentrations in quartz, and petrographic textures indicating deformation, recrystallization, and residence at elevated P–T conditions (undulose extinction in quartz, subgrains, serrated grain boundaries, and grain coarsening) support final equilibration in the deep crust at unusually high temperatures. U–Pb and Hf isotopes in detrital zircons yield discordia wherein U–Pb upper intercepts represent variable crystallization ages indicative of ancient (>1 Ga) North American basement, but a common lower intercept at 103 ± 10 Ma, coinciding with peak arc magmatism in the Western US Cordillera.

We propose three hypotheses by which the quartzites were transported into the lower crust. The first involves underthrusting of continental crust beneath the arc. Detrital zircon provenances are consistent with origin of the quartzites as passive margin sediments deposited in the upper continental plate. The common lower intercept coincident with peak arc magmatism indicates that the quartzites were within the lower crust by that time, but we cannot further resolve whether underthrusting was pre-magmatic or syn-magmatic. The second hypothesis involves downwelling of wallrocks in response to pluton diapirism, but the amount of displacement needed, insufficient density contrast, and debate concerning diapirism or diking as the dominant pluton ascent mechanism add uncertainty to this scenario. Finally, the third hypothesis considers felsic relamination of the lower crust by buoyant sediment diapirs derived from the downgoing slab. The ubiquity of passive margin provenances rather than "active margin" (trench, accretionary prism) sources in the detrital zircons is difficult to reconcile with this hypothesis.

Regardless of what mechanism transported the quartzites beneath the arc, the fact that they are present in what presumably is a predominantly mafic lower crust has significant implications for the compositional and tectonic history of the continental crust. The Sierran quartzites are evidence that the lower crust may be more felsic than previously thought. Melting models suggest that the quartzites could be residues of partial melting of impure quartzitic protoliths. Even under water-saturated conditions, such protoliths yield far less melt compared to pelitic lithologies at the same temperature. Thus, the refractory and infertile nature of quartzites could allow them to persist in the lower crust. Currently, the abundance of felsic rocks in the lower crust is poorly constrained, although a recent analysis by Hacker et al. (2011) suggested >10–20% of pelites in the lower crust might be permissible.

Lastly, if the Sierran quartzites represent underthrusted continental upper plate, this has implications for tectonic processes operating in continental arcs. One implication is that underthrusting thickens the continental lithosphere and affects its overall composition if felsic upper crustal rocks are transported into the deep crust. Thickening and underthrusting might be facilitated during periods of intensified arc magmatism, as higher temperatures associated with deep crustal melting could potentially trigger weakening of the lower crust and enhance lower crustal decollements. Thus, arc magmatism and tectonic thickening may go hand in hand in continental arcs.

Acknowledgments

The authors are indebted to Jade Star Lackey, Oliver Jagoutz, Mihai Ducea for constructive and critical reviews, and to Editor T. Mark Harrison for his efficient handling of the manuscript. Ray Guillemette provided invaluable help in the electron microprobe laboratory at Texas A&M University. We also thank Mike Tice for help using the XRF microanalyzer at Texas A&M University. This research was supported by NSF EAR 1119315 grant to C.-T.A.L. Funding for the instruments used in this study at UC Davis are provided by the University of California Davis start-up funds and NASA's Planetary Major Equipment grants (NNG05GN03G and NNX08AG57G) to Q.-Z.Y. State Key Laboratory of Lithospheric Evolution, IGG-CAS Grants Z201003 and Z0802 have enabled the participation of LWX in this project.

Appendix A. Supplementary materials

Supplementary data associated with this article can be found in the online version at http://dx.doi.org/10.1016/j.epsl.2012.11.031.

References

Annen, C., Blundy, J.D., Sparks, R.S.J., 2006. The genesis of intermediate and silicic magmas in deep crustal hot zones. J. Petrol. 47, 505–539.

Armstrong, R.L., 1968. The Cordilleran miogeosyncline in Nevada and Utah. Utah Geol. Mineral. Surv. Bull. 78, 58.

Barbeau, D.L., Ducea, M.N., Gehrels, G.E., Kidder, S., Wetmore, P.H., Saleeby, J.B., 2005. U–Pb detrital-zircon geochronology of northern Salinian basement and cover rocks. Geol. Soc. Am. Bull. 117, 466–481.

Behn, M.D., Kelemen, P.B., Hirth, G., Hacker, B.R., Massonne, H.J., 2011. Diapirs as the source of the sediment signature in arc lavas. Nat. Geosci. 4, 641–646.

Bennett, V.C., DePaolo, D.J., 1987. Proterozoic crustal history of the western United States as determined by neodymium isotopic mapping. Geol. Soc. Am. Bull. 99, 674–685.

Black, L.P., Kamo, S.L., Allen, C.M., Aleinikoff, J.N., Davis, D.W., Korsch, R.J., Foudoulis, C., 2003. TEMORA 1: a new zircon standard for Phanerozoic U–Pb geochronology. Chem. Geol. 200, 155–170.

Bouvier, A., Vervoort, J.D., Patchett, P.J., 2008. The Lu–Hf and Sm–Nd isotopic composition of CHUR: constraints from unequilibrated chondrites and implications for the bulk composition of terrestrial planets. Earth Planet. Sci. Lett. 273, 48–57.

Bucher, K., Frey, M., 1994. Petrogenesis of metamorphic rocks. Springer-Verlag, Berlin, Heidelberg.

Chen, J.H., Moore, J.G., 1982. Uranium–lead isotopic ages from the Sierra Nevada Batholith, California. J. Geophys. Res. 87, 4761–4784.

Chin, E.J., Lee, C.-T.A., Luffi, P., Tice, M., 2012. Deep lithospheric thickening and refertilization beneath continental arcs: case study of the P, T and compositional evolution of peridotite xenoliths from the Sierra Nevada, California. J. Petrol. 53, 477–511.

Clemens, J.D., Vielzeuf, D., 1987. Constraints on melting and magma production in the crust. Earth Planet. Sci. Lett. 86, 287–306.

Coleman, D.S., Glazner, A.F., 1997. The Sierra crest magmatic event: rapid formation of juvenile crust during the Late Cretaceous in California. Int. Geol. Rev. 39, 768–787.

de Capitani, C., Petrakakis, K., 2010. The computation of equilibrium assemblage diagrams with Theriak/Domino software. Am. Mineral. 95, 1006–1016.

DeCelles, P.G., Ducea, M.N., Kapp, P., Zandt, G., 2009. Cyclicity in Cordilleran orogenic systems. Nat. Geosci. 2, 251–257.

Dickinson, W.R., 1981. Plate tectonics and the continental margin of California. In: Ernst, W.G. (Ed.), The Geotectonic Development of California. Prentice-Hall, Englewood Cliffs, New Jersey, pp. 1–28.

Dodge, F.C.W., Lockwood, J.P., Calk, L.C., 1988. Fragments of the mantle and crust from beneath the Sierra Nevada batholith: xenoliths in a volcanic pipe near Big Creek, California. Geol. Soc. Am. Bull. 100, 938–947.

Ducea, M., Barton, M.D., 2007. Igniting flare-up events in Cordilleran arcs. Geology 35, 1047–1050.

Ducea, M.N., Saleeby, J.B., 1996. Buoyancy sources for a large, unrooted mountain range, the Sierra Nevada, California: evidence from xenolith thermobarometry. J. Geophys. Res. 101, 8229–8244.

Ducea, M.N., Saleeby, J.B., 1998. The age and origin of a thick mafic–ultramafic keel from beneath the Sierra Nevada batholith. Contrib. Mineral. Petrol. 133, 169–185.

England, P.C., Thompson, A., 1986. Some thermal and tectonic models for crustal melting in continental collision zones, 19. Geological Society, Special Publications, London, pp. 83–94.

Gehrels, G.E., Dickinson, W.R., Ross, G.M., Stewart, J.H., Howell, D.G., 1995. Detrital zircon reference for Cambrian to Triassic miogeoclinal strata of western North America. Geology 23, 831–834.

Girty, G.H., Hanson, A.D., Knaack, C., Johnson, D., 1994. Provenance determined by REE, Th, and Sc analyses of metasedimentary rocks, Boyden Cave roof pendant, central Sierra Nevada, California. J. Sediment. Res. 64, 68–73.

Grasse, S.W., Gehrels, G.E., Lahren, M.M., Schweickert, R.A., Barth, A.P., 2001. U–Pb geochronology of detrital zircons from the Snow Lake pendant, central Sierra Nevada Implications for Late Jurassic Early Cretaceous dextral strike-slip faulting. Geology 29, 307–310.

Gualda, G.A.R., Ghiorso, M.S., Lemons, R.V., Carley, T.L., 2012. Rhyolite-MELTS: a modified calibration of MELTS optimized for silica-rich, fluid-bearing magmatic systems. J. Petrol. 53 (5), 875–890.

Hacker, B.R., Kelemen, P.B., Behn, M.D., 2011. Differentiation of the continental crust by relamination. Earth Planet. Sci. Lett. 307, 501–516.

Hanchar, J.M., Miller, C.F., Wooden, J.L., Bennett, V.C., Staude, J.-M.G., 1994. Evidence from Xenoliths for a dynamic lower crust, Eastern Mojave Desert, California. J. Petrol. 35, 1377–1415.

Hildreth, W., 1981. Gradients in silicic magma chambers: implications for lithospheric magmatism. J. Geophys. Res. 86, 10153–10192.

Hildreth, W., Moorbath, S., 1988. Crustal contributions to arc magmatism in the Andes of Central Chile. Contrib. Mineral. Petrol. 98, 455–489.

Hoskin, P.W.O., Black, L.P., 2000. Metamorphic zircon formation by solid-state recrystallization of protolith igneous zircon. J. Metamorph. Geol. 18, 423–439.

Jackson, S.E., Pearson, N.J., Griffin, W.L., Belousova, E.A., 2004. The application of laser ablation-inductively coupled plasma-mass spectrometry to in situ U–Pb zircon geochronology. Chem. Geol. 211, 47–69.

Jessell, M.W., 1987. Grain-boundary migration microstructures in a naturally deformed quartzite. J. Struct. Geol. 9, 1007–1014.

Kistler, R.W., 1990. Two different lithosphere types in the Sierra Nevada, California. In: Anderson, J.L. (Ed.), The Nature and Origin of Cordilleran Magmatism. Geological Society of America, Boulder, CO, pp. 271–281.

Kistler, R.W., Peterman, Z.E., 1973. Variations in Sr, Rb, K, Na, and Initial Sr87/Sr86 in Mesozoic granitic rocks and intruded wall rocks in Central California. Geol. Soc. Am. Bull. 84, 3489–3512.

Koziol, A.M., Newton, R.C., 1988. Redetermination of the anorthite breakdown reaction and improvement of the plagioclase–garnet–Al_2SiO_5–quartz geobarometer. Am. Mineral. 73, 216–223.

Lackey, J.S., Cecil, M.R., Windham, C.J., Frazer, R.E., Bindeman, I.N., Gehrels, G.E., 2012. The fine gold intrusive suite: the roles of basement terranes and magma source development in the Early Cretaceous Sierra Nevada batholith. Geosphere 8, 292–313.

Lee, C.-T., Rudnick, R.L., Brimhall Jr., G.H., 2001. Deep lithospheric dynamics beneath the Sierra Nevada during the Mesozoic and Cenozoic as inferred from xenolith petrology. Geochem. Geophys. Geosyst. 2 (12), 1053, http://dx.doi.org/10.1029/2001GC000152.

Lee, C.-T., Yin, Q., Rudnick, R.L., Chesley, J.T., Jacobsen, S.B., 2000. Osmium isotopic evidence for mesozoic removal of lithospheric mantle beneath the Sierra Nevada, California. Science 289, 1912–1916.

Lee, C.-T.A., Cheng, X., Horodyskyj, U., 2006. The development and refinement of continental arcs by primary basaltic magmatism, garnet pyroxenite accumulation, basaltic recharge and delamination: insights from the Sierra Nevada. Contrib. Mineral. Petrol. 151, 222–242.

Ludwig, K.R., 2003. ISOPLOT: a Geochronological Toolkit for Microsoft Excel 3.0. Berkeley Geochronology Center Special Publication no. 4.

McDonough, W.F., Sun, S.S., 1995. The composition of the Earth. Chem. Geol. 120, 223–253.

Moore, J.N., Foster Jr., C.T., 1980. Lower Paleozoic metasedimentary rocks in the east-central Sierra Nevada, California: correlation with Great Basin formations. Geol. Soc. Am. Bull. 91, 37–43.

Mukhopadhyay, B., Manton, W.I., 1994. Upper-mantle fragments from beneath the Sierra Nevada Batholith: partial fusion, fractional crystallization, and metasomatism in a subduction related ancient lithosphere. J. Petrol. 35, 1417–1450.

Nemchin, A.A., Giannini, L.M., Bodorkos, S., Oliver, N.H.S., 2001. Ostwald ripening as a possible mechanism for zircon overgrowth formation during anatexis: theoretical constraints, a numerical model, and its application to pelitic migmatites of the Tickalara Metamorphics, northwestern Australia. Geochim. Cosmochim. Acta 65, 2771–2788.

Oldow, J.S., Bally, A.W., Ave-Lallemant, H.G., 1990. Transpression, orogenic float, and lithospheric balance. Geology 18, 991–994.

Petford, N., 1996. Dykes or diapirs? Earth Environ. Sci. Trans. R. Soc. Edinburgh 87, 105–114.

Rubatto, D., Williams, I.S., Buick, I.S., 2001. Zircon and monazite response to prograde metamorphism in the Reynolds Range, central Australia. Contrib. Mineral. Petrol. 140, 458–468.

Rudnick, R.L., Fountain, D.M., 1995. Nature and composition of the continental crust: a lower crustal perspective. Rev. Geophys. 33, 267–309.

Rudnick, R.L., McDonough, W.F., O'Connell, R.J., 1998. Thermal structure, thickness and composition of continental lithosphere. Chem. Geol. 145 (3), 395–411.

Saleeby, J., Ducea, M., Clemens-Knott, D., 2003. Production and loss of high-density batholithic root, southern Sierra Nevada, California. Tectonics 22, 1064.

Seeland, D.A., 1968. Paleocurrents of the Late Precambrian to Early Ordovician (Basal Sauk) Transgressive Clastics of the Western and Northern United States. Masters Thesis. University of Utah, 276 p.

Shelley, D., 1993. Igneous and Metamorphic Rocks Under the Microscope: Classification, Textures, Microstructures, and Mineral Preferred Orientations. Chapman & Hall, London.

Slama, J., Kosler, J., Condon, D.J., Crowley, J.L., Gerdes, A., Hanchar, J.M., Horstwood, M.S.A., Morris, G.A., Nasdala, L., Norberg, N., Schaltegger, U., Schoene, B., Tubrett, M.N., Whitehouse, M.J., 2008. Plesovice zircon—a new natural reference material for U–Pb and Hf isotopic microanalysis. Chem. Geol. 249, 1–35.

Spear, F.S., 1995. Metamorphic phase equilibria and pressure–temperature–time paths, second ed. Mineralogical Society of America.

Springer, M., Forster, A., 1998. Heat-flow density across the Central Andean subduction zone. Tectonophysics 291, 123–139.

Stern, R.A., Amelin, Y., 2003. Assessment of errors in SIMS zircon U–Pb geochronology using a natural zircon standard and NIST SRM 610 glass. Chem. Geol. 197, 111–142.

Stern, T.W., Bateman, P.C., Morgan, B., Newell, M.F., Peck, D.L., 1981. Isotopic U–Pb Ages of Zircon from the Granitoids of the Central Sierra Nevada, California. USGS Professional Paper 1185, 19.

Stewart, J.H., 1970. Upper Precambrian and Lower Cambrian Strata in the Southern Great Basin, California and Nevada: US Geological Survey Professional Paper 620, 206.

Suppe, J., 1985. Principles of Structural Geology. Prentice Hall, Englewood Cliffs, NJ.

Tilton, G.R., 1960. Volume diffusion as a mechanism for discordant Lead ages. J. Geophys. Res. 65, 2933–2945.

Tollstrup, D.L., Xie, L.-W., Wimpenny, J., Chin, E.J., Lee, C.-T., Yin, Q., 2012. A trio of laser-ablation in concert with two ICP-MSs: simultaneous, pulse-by-pulse determination of U–Pb discordant ages and a single spot Hf isotope ratio analysis in complex zircons from petrographic thin sections. Geochem. Geophys. Geosyst. 13, Q03017 (14 pp), http://dx.doi.org/10.1029/2011GC004027.

Vavra, G., Gebauer, D., Schmid, R., Compston, W., 1996. Multiple zircon growth and recrystallization during polyphase Late Carboniferous to Triassic metamorphism in granulites of the Ivrea Zone (Southern Alps): an ion microprobe (SHRIMP) study. Contrib. Mineral. Petrol. 122, 337–358.

Vervoort, J.D., Blichert-Toft, J., 1999. Evolution of the depleted mantle: Hf isotope evidence from juvenile rocks through time. Geochim. Cosmochim. Acta 63, 533–556.

Wark, D., Watson, E., 2006. TitaniQ: a titanium-in-quartz geothermometer. Contrib. Mineral. Petrol. 152, 743–754.

Watson, E.B., Harrison, T.M., 1983. Zircon saturation revisited: temperature and composition effects in a variety of crustal magma types. Earth Planet. Sci. Lett. 64, 295–304.

Wickham, S.M., 1987. Crustal Anatexis and granite petrogenesis during low-pressure regional metamorphism: the Trois Seigneurs Massif, Pyrenees, France. J. Petrol. 28, 127–169.

Wiedenbeck, M., Alle, P., Corfu, F., Griffin, W.L., Meier, M., Oberli, F., Quadt, A.V., Roddick, J.C., Spiegel, W., 1995. Three natural Zircon standards for U–Th–Pb, Lu–Hf, trace element and REE analyses. Geostand. Newsl. 19, 1–23.

Xie, L., Zhang, Y., Zhang, H., Sun, J., Wu, F., 2008. In situ simultaneous determination of trace elements, U–Pb and Lu–Hf isotopes in zircon and baddeleyite. Chin. Sci. Bull. 53, 1565–1573.

Zeng, L., 2004. Non-Modal Partial Melting of Metasedimentary Pendants in the Southern Sierra Nevada and Implications for the Deep Origin of Within-Pluton Isotopic Heterogeneity, Ph.D. Thesis. California Institute of Technology, 220 p.